Chapter 4

Effect of Time Correlated Gains [*]

In this chapter, we study the effect of time-correlated residual gain errors in high dynamic range observations, such as that for 21- cm signal from EoR. We address the problem by modeling time-dependent residual gain errors directly and investigate the systematics that may arise in the observations of the redshifted 21-cm emission in the presence of bright foreground, a particular antenna configuration, and a gain model. We considered the gain models with time-correlated residual gain errors, where residual gain errors are modeled using a power-law function. Although the gain errors depend on time and frequency, we do not consider the frequency dependence of the gain, and the whole analysis is done for a single frequency channel only. The effect of frequency dependence of the gain errors will be discussed in a later chapter.

4.1 Gain error model

In radio interferometric observations, each antenna of a radio interferometer records the electric fields incident on its cross dipoles modified by the complex gain arising from the entire electronic chain. In addition to the electronic chain, the ionosphere also adds to the

---

[*] The content in this chapter is originally presented in Kumar et al. (2020)

complex gain. Later these electric field signals are correlated to give visibility. While doing the data analysis, with the help of primary calibrators and the self-calibration method, the antenna gains are calculated as a function of time, and the visibilities are calibrated for the complex gains and prepared for further analysis. Note that the gain calibration can only be done to certain accuracy depending on the quality of the primary calibrators, receiver noise, ionospheric stability, etc. We shall refer to the uncalibrated part of the gain as residual gain. The residual complex gain from antenna A can be modeled as

$$\tilde{g}_A(t) = [1+\delta_A(t)]\, e^{i\phi_A(t)}, \tag{4.1}$$

where both δ_A and ϕ_A are much smaller than unity and randomly distributed. Here we do not consider the frequency dependence of the gain, hence the frequency dependence of the gains is not written explicitly.

The visibility $\tilde{V}^M_{AB}(t)$ measured by antenna pair A and B in the presence of the residual gain can be written in terms of the visibility function from the sky $V^S_{AB} =< E^*_A E_B >$ as

$$\tilde{V}^M_{AB}(t) =< [1+\delta_A(t)]\,[1+\delta_B(t)]\, e^{i(\phi_B(t)-\phi_A(t))} > V^S_{AB}. \tag{4.2}$$

Here a primary assumption used is that the specific intensity, and hence the visibility function of the source is independent of time (Taylor et al., 1999). Clearly, the excess or the residual visibility recorded by the interferometer due to the residual gain error can be written as

$$\tilde{V}^R_{AB}(t) = \tilde{V}^M_{AB}(t) - V^S_{AB}. \tag{4.3}$$

We assume that the quantities $\delta_A(t)$ and $\phi_A(t)$, which characterize the residual gain errors, follow Gaussian distribution with mean zero. Here we assume that the residual gain errors are uncorrelated in frequency and consider the effect of time correlation only, hence the frequency dependence of the gains is not written explicitly. Small asymmetry in the antenna beam pattern, parallactic angle rotation, and time coherence in the electron density variation in the ionosphere are expected to introduce time correlation in the residual gains. We quantify this time correlation using two-point correlation functions of $\delta_A(t)$ and $\phi_A(t)$ as

$$\begin{aligned}
\xi_{\delta A}(\tau) &= \langle \delta_A(t)\delta_A(t+\tau)\rangle, \quad \sigma_{\delta A}^2 = \langle \delta_A^2 \rangle \\
\xi_{\phi A}(\tau) &= \langle \phi_A(t)\phi_A(t+\tau)\rangle, \quad \sigma_{\phi A}^2 = \langle \phi_A^2 \rangle,
\end{aligned} \tag{4.4}$$

were $\xi_A(t) = 0 \; \forall \; \tau \neq 0$ corresponds to the case of no time correlation. We have assumed the parameters σ is independent of frequency, the residual gain errors from different antennae are uncorrelated and there is no correlation between the amplitude and the phase gain errors of any antenna. In general, the correlation properties of the residual gain from the different antennas are expected to be different. To simplify, we assume that the correlation properties of all the antennae are the same and hence the antenna indices can be dropped from the above expressions. The auto-correlation function of residual gain components can be expressed alternatively in terms of the time-averaged correlations χ_δ and χ_ϕ defined as

$$\begin{aligned}
\chi_\delta(T_D) &= \frac{1}{T_D}\int_0^{T_D} \xi_\delta(t)\mathrm{d}t \qquad (4.5)\\
\chi_\phi(T_D) &= \frac{1}{T_D}\int_0^{T_D} \xi_\phi(t)\mathrm{d}t,
\end{aligned}$$

which are particularly useful as the ensemble average in equation 4.4 is performed assuming the system is intermittent. Here T_D corresponds to the averaging time used to correlate the visibilities.

4.2 Power spectrum estimation and bias

The statistical nature of the signal is quantified by the power spectrum of the sky brightness distribution. Bharadwaj and Sethi (2001) have shown that the power spectrum of the sky brightness distribution can be estimated directly by correlating the visibilities at the same baselines. We have neglected the receiver noise in equation 4.2. In most radio interferometric observations, the receiver noise dominates the visibility measurements. Bharadwaj and Ali (2005) has observed that the noise is not correlated across nearby baselines, but the sky signal is correlated. Based on this, they proposed that the real part of the visibility correlation at nearby baselines can be used as the power spectrum estimator

$$\mathscr{E}[P(\vec{U})] = \mathscr{R}e\left[\langle V(\vec{U})^{*}V(\vec{U}+\Delta\vec{U})\rangle\right]. \tag{4.6}$$

Here, the angular brackets denote the ensemble average.
We use the visibility-based power spectrum estimator that requires performing an ensemble average over many realizations of the visibility correlation at a given baseline vector. Since we always have only one realization of the observed sky, the ensemble average is done assuming spatial ergodicity. Each antenna has a finite response over the sky. This correlates the observed signal in the nearby baselines, and we may consider the visibility correlations performed over a small region near a given baseline vector as different realizations. The real part of the average of these realizations is then taken as the estimate of the power spectrum at that baseline.

The presence of residual gain errors may introduce an additional bias in the estimation of the power spectrum by visibility correlation. This bias depends explicitly on the time and the antenna pair involved in the visibility measurements. The contribution to the bias from a particular visibility correlation $V2$ can be written in terms of the residual visibilities (see equation 4.3) as

$$V2^R_{ABCD}(\vec{U},t,\vec{U}+\Delta\vec{U},t') = \tilde{V}^R_{AB}(\vec{U},t)^* \, \tilde{V}^R_{CD}(\vec{U}+\Delta\vec{U},t'). \tag{4.7}$$

In general, different combinations of antenna pairs, e. g. antenna pair AB with antenna pair CD, etc., can give rise to nearby baseline vectors. The bias in the power spectrum is the average of all the $V2^R$ from all the possible antenna pairs giving rise to the nearby baseline vectors. For the power spectrum estimator discussed here, the ensemble average in equation (4.6) is estimated over all the visibility measurements in a circular region of radius $\mid \Delta\vec{U} \mid$ at the baseline $\vec{U}$. The visibility correlations performed to estimate the power spectrum at the baseline $\vec{U}$ will have four different types of contributions from these visibility measurements. These are correlations of baselines assumed by the same antenna at different times, correlations of baselines with one common antenna at the same or different time stamps, and correlations of baselines assumed by all four different antennae at the same or different time stamps. Since we do not expect any correlation in the residual gains across the different antennae, the residual gain correlation is important only when at least one antenna is common between the two baselines correlated. These cases are discussed below.

- **Case I** Same antenna pairs correlated at different times: Here we consider the correlation of the same antenna pairs, say AB, at different time stamps of observations to get nearby baseline vectors, i.e,

  $$V2^R_{ABAB}(\vec{U},t,\vec{U}+\Delta\vec{U},t') = \tilde{V}^R_{AB}(\vec{U},t)^* \, \tilde{V}^R_{AB}(\vec{U}+\Delta\vec{U},t'). \tag{4.8}$$

  If in the region in the baseline plane over which the visibility correlation is performed to estimate the power spectrum at a given baseline, only these types of baselines are present, the ensemble averaging to estimate the power spectrum from visibility correlation is replaced with a time average. The averaging time is directly related to the dimension of the region in baseline space over which the average is performed, the particular baseline value, as well as the source declination, and telescope latitude. In general, any pair of antennae traces elliptical tracks in the $u-v$ plane because of the earth's rotation. For the purpose of this discussion, we take a very simplistic model where the antenna pairs AB makes a circular arc of radius $U =\mid \vec{U} \mid$ in the baseline plane with center at $\vec{U} = 0$ and makes a complete circle in 24 hours. The averaging time T_D is then the time the antenna pair stays within the region of width $\Delta U =\mid \Delta\vec{U} \mid$ over which the nearest baseline averaging is done. Hence, $T_D = \frac{\Delta U\ T_{24}}{\pi U}$, where T_{24} is the time in a day. Usually, the values of ΔU are kept constant for the entire baseline plane; hence, $T_D \propto \frac{1}{U}$. Assuming the gain model given in section 4.1 and neglecting all high-order correlations, the residual power spectrum for this case can be written as

$$P_I^R(\vec{U}) = [2\chi_\delta(T_D) + 2\chi_\phi(T_D)]P^S(\vec{U}), \tag{4.9}$$

where $P^S(\vec{U})$ is the power spectrum of the sky brightness distribution. Let us assume that $n_I(\vec{U})$ gives the fraction baseline pairs of this type available within the correlation region. Note that, $n_I(\vec{U})$ depends on the baseline distribution.

- **Case II** Baseline pairs with only one common antenna, correlated at the same time: Here we consider the correlation of the baselines where one antenna is common between them, say AB and antenna AC are correlated at the same time stamps of observations to get nearby baseline vectors, i.e,

$$V2^R_{ABAC}(\vec{U},t,\vec{U}+\Delta\vec{U},t) = \tilde{V}^R_{AB}(\vec{U},t)^*\ \tilde{V}^R_{AC}(\vec{U}+\Delta\vec{U},t). \tag{4.10}$$

Since, in this case, different time correlations between the baselines are not involved, the residual power spectrum does not depend on the auto-correlation functions of the gain. The residual power spectrum can be given as

$$P^R_{II}(\vec{U}) = [\sigma_\delta^2 + \sigma_\phi^2] P^S(\vec{U}). \tag{4.11}$$

Let us assume that the fraction of such baseline pairs available within the correlation region is $n_{II}(\vec{U})$.

- **Case III** Baseline pairs with only one common antenna, correlated at different times: This is the same as the case above but the correlation is done at different time stamps of observations to get nearby baseline vectors, i.e,

  $$V2^R_{ABAC}(\vec{U}, t, \vec{U} + \Delta\vec{U}, t') = \tilde{V}^R_{AB}(\vec{U}, t)^* \, \tilde{V}^R_{AC}(\vec{U} + \Delta\vec{U}, t'). \tag{4.12}$$

  The residual power spectrum can be written as

  $$P^R_{III}(\vec{U}) = [\chi_\delta(T_D) + \chi_\phi(T_D)] P^S(\vec{U}), \tag{4.13}$$

  and the fraction of such baseline pairs available within the correlation region is $n_{III}(\vec{U})$.

- **Case IV** Baseline pairs with no common antenna: In the correlation regions, we also expect to perform the correlation between baseline pairs with no antenna in common. These visibility correlations will have zero residual power spectrum with our present assumptions.

We assume that the auto-correlation functions and hence the χ_δs have power-law dependence in time, that is $\chi_\delta(T_D) = \Delta_0 T_D^{-\alpha_\delta}$ and $\chi_\phi(T_D) = \nabla_0 T_D^{-\alpha_\phi}$. For simplicity we consider that $\sigma_\delta = \sigma_\phi = \sigma$, $\Delta_0 = \nabla_0$ and $\alpha_\delta = \alpha_\phi = \alpha$. These simplifications are just to reveal the effect of baseline distribution. Note that for $\alpha = 0$, the correlation time in the residual gain error is practically infinite, whereas $\alpha = 1$ corresponds to very little correlation in time.

With the above simplification, the bias in the visibility correlation estimator arising due to the residual gain errors can be written as

$$\mathscr{B}[P](\vec{U}) = \left(\left[4n_I(\vec{U}) + 2n_{III}(\vec{U})\right]\Lambda_0 U^{\alpha} + 2n_{II}(\vec{U})\sigma^2\right) P^S(\vec{U}), \tag{4.14}$$

where $\Lambda_0 = \frac{\Delta_0\ \Delta U\ T_{24}}{\pi}$. Clearly, bias is multiplicative. We define the ratio of the bias to the sky power spectrum as the power spectral gain,

$$\mathscr{G}(\vec{U}) = \mathscr{B}[P](\vec{U})/P^S(\vec{U}), \tag{4.15}$$

which depends on the residual gain errors and the baseline distribution and is independent of the contribution from the sky. Note that the definition of the power spectral gain is independent of the gain error and baseline distribution models.

4.3 A toy model of baseline pair fractions

In order to understand the effect of various factors in the residual power spectrum, we consider the following two simplistic models for the baseline pair distributions here. Firstly, we assume different baseline pair fractions are the same, i.e,

$$n_I = n_{II} = n_{III} = n_{IV} = \frac{1}{4}. \tag{4.16}$$

For this model of baseline pair fractions, the bias in the visibility correlation becomes

$$\mathscr{B}[P](\vec{U} = \left[\frac{3}{2}\Lambda_0 U^{\alpha} + \frac{1}{2}\sigma^2\right] P^S(\vec{U}), \tag{4.17}$$

To access the effect of n_i in the power spectrum bias in a more realistic situation we consider

$$n_i(U) = \frac{\exp\left[-(\gamma_i U)^2\right]}{\sum_i \exp\left[-(\gamma_i U)^2\right]}, \tag{4.18}$$

where N_0 and γ_i are constants. It is expected that at the long baselines, the contribution will be more from the baseline pairs of type I, etc., that is, $\gamma_1 < \gamma_2 < \gamma_3 < \gamma_4$.

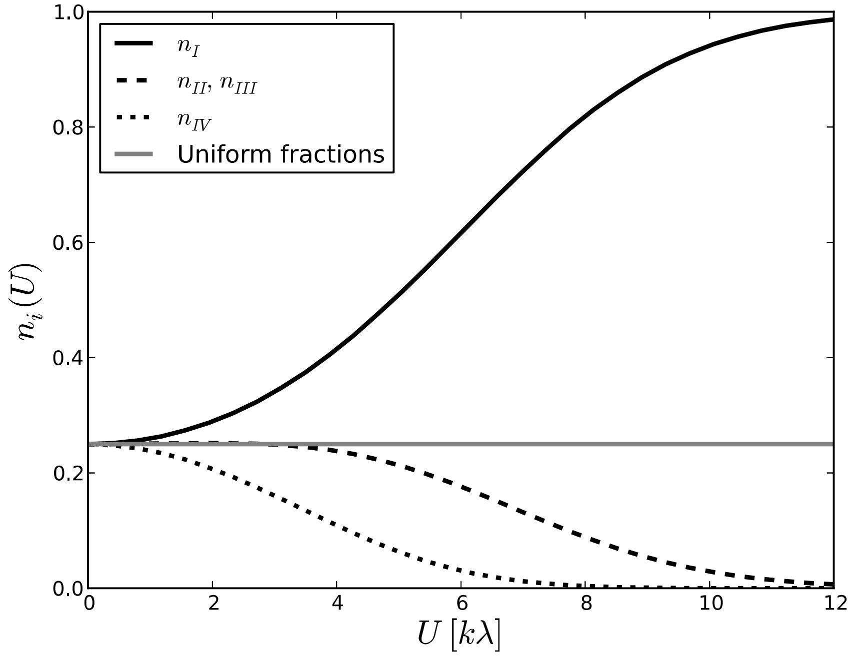

Fig. 4.1 Models for different baseline pair distributions are shown as a function of baseline for an array with a maximum baseline of 12 kλ. The quantities n_i correspond to a fraction of baseline pairs of a particular kind as discussed in section 4.2. The horizontal grey line corresponds to the case when all types of baseline pairs have the same proportions.

Variation of the baseline pair fractions n_i as a function of distance from the center of the baseline plane (U) is shown in figure 4.1. The horizontal grey line corresponds to the case of uniform fraction given in equation (4.16). The solid black, dashed and dot-dashed lines correspond to n_I, n_2, n_3, and n_4 respectively. We have chosen $\gamma_1 = 1/6$, $\gamma_2 = \gamma_3 = 1/4$ and $\gamma_4 = 1/3$ in this plot. Clearly, all four types have similar contributions at the smallest baselines, whereas at the largest baseline, only the baseline pairs discussed in case I contribute. As can be seen, the residual gain errors have two effects on the bias in the power spectrum estimates. Firstly, for the same range of visibility correlation ΔU, the time correlation in gain error affects the long baselines more than the smaller baselines. On the other hand, the fraction of baseline pairs of type I, which produces relatively more bias in the power spectrum estimates, comes in a larger fraction at the long baselines. These two effects sum up and produce baseline-based bias in the power spectrum estimates. We

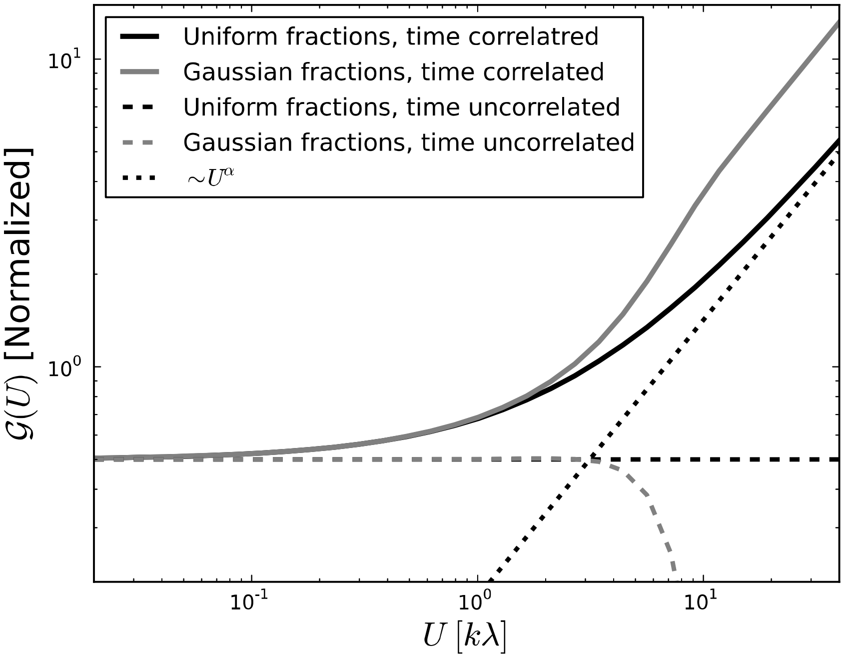

Fig. 4.2 Power spectral gain is plotted as a function of baselines (solid lines) for two types of baseline pair fractions discussed in the text. The values in the y axis are normalized by the standard deviation of the gain errors. The horizontal dashed line corresponds to the case when there is no time correlation in the residual gain errors. The dot-dashed line is parallel to the auto-correlation spectra of the gain errors (see text for details). A significant change in the power spectra is expected for such time-correlated gain errors.

use equation 4.14 along with the two models for the baseline pair distribution to estimate the bias in the power spectrum estimates. Figure 4.2 plots the bias in the power spectrum estimates as a function of baselines. The bias is normalized by $\sigma^2 P^S(U)$. We have taken the value of $\alpha = 0.9$. The dark black line corresponds to the case with the uniform baseline pair fraction. For this case, at the short baselines, the normalized bias is almost constant at a value of $1/2$ and assumes a power-law parallel to U^{α} at long baselines (dot-dashed line). The solid grey line corresponds to the case with the baseline pair fractions corresponding to equation 4.18. Clearly, an extra steepening of the bias, due to the presence of a large fraction of baseline pair of type I at the long baselines, is seen. The dashed lines correspond to the cases when there is no time correlation in the residual gain errors. The uniform baseline pair fraction is shown in dark black, and the baseline pair fractions as given by equation 4.16 are shown in grey. These toy models demonstrate that the bias in the power spectrum originating from the residual gain error is scale (or baseline) dependent. The bias-to-signal ratio in the power spectrum estimates is directly proportional to the standard deviation of the residual gain errors and limits the dynamic range to which the estimated power spectrum has statistical significance. Clearly, if residual gain errors are smaller than unity, any signal is always larger than the bias produced for its presence.

4.4 Residual Gain Errors in presence of extragalactic point sources

We investigate the effect of time-correlated residual gain errors in the measurement of the redshifted 21-cm power spectrum in the presence of bright foreground sources. We use bright, compact sources as our foreground model. We model the source distributions from their observed differential source count. The clustering of the compact sources is neglected here. The bias in the power spectrum arising from residual gain errors and the compact extragalactic sources are expected to be several orders of magnitude higher than the expected redshifted 21-cm signal. Since the 21-cm signal itself is expected to be quite low compared to that from the compact sources, we have neglected its own bias.

4.4.1 Point source sky model

The number of sources in a flux density range S and $S+\mathrm{d}S$ per unit solid angle in the sky for a given field of view of observation is defined by the quantity $\frac{\mathrm{d}N}{\mathrm{d}S}$, known as the differential source count. The gross variation of flux density of radio sources is expressed in terms of the spectral index. The flux density of a given source as F_1 and F_2 at frequencies ν_1 and ν_2, the spectral index is defined as $-\frac{log(F_1/F_2)}{log(\nu_1/\nu_2)}$.

The 21-cm signal from the epoch of reionization is expected to be redshifted to ~ 100 MHz and higher. Hence we are interested in source statistics near this frequency band. Differential source counts at ~ 150 MHz have been calculated from various surveys in the literature. These include source counts from a single deep GMRT integration, and a larger-area GMRT survey centered on the Boötes field (Intema et al., 2011; Williams et al., 2016), from the 7C survey (Hales et al., 2007; McGilchrist et al., 1990), from deep, small-area surveys with the LOFAR HBA system Hardcastle et al. (2016); Mahony et al. (2016); Williams et al. (2016), from the MWA GLEAM survey (Wayth et al., 2015) as well as from deep but single-pointing MWA survey Franzen et al. (2016, 2019); Hurley-Walker et al. (2016), etc. Intema et al. (2017) has used the entire TGSS survey to estimate the differential source count at 150 MHz based on the TGSS-ADR1 (Intema et al., 2017). Because of the large sky coverage and hence a large number of statistics, the TGSS ADR1 provides strict constraints on the shape of the source count distribution over the relevant flux density range. In this work, we use the source counts from TGSS ADR1, where the differential source count is expressed over the flux density range of 5 mJy to 100 Jy as

$$log_{10}(S^{5/2}dN/dS) = C_0 + \sum_{i=1}^{5} C_i \times [log_{10}(S)]^i. \tag{4.19}$$

Here $C_i^{\prime}s$ are constants, values are given in Intema et al. (2017). Intema et al. (2017) have also reported the spectral index of the sources in the TGSS ADR1. Their reported spectral index distribution can be well approximated with a Gaussian distribution with a mean of -0.73 with the top and bottom 10 percent of the sources lying beyond 0.43 and -1.0. Tiwari (2019) has extensively investigated the spectral index distribution of the sources in TGSS ADR1. They find for (all the sources) the mean spectral index is -0.7 with a dispersion of 0.2. We use a Gaussian distribution of the spectral index with a mean of -0.7 and a standard deviation of 0.2 to generate a point source sky model at the desired frequency.

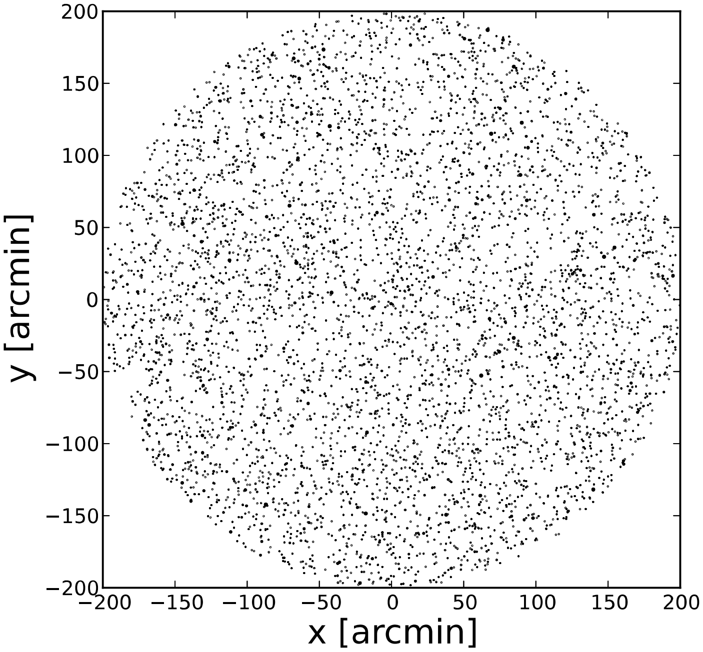

Fig. 4.3 The point source foreground. x and y are the x positions and y positions of the sources from the pointing center in arcmin.

4.4.2 Simulation method

We have demonstrated the effect of baseline pair distribution on the bias in the power spectrum estimation in section 4.2 using a toy model for the telescope baseline pair distribution. It is expected that the residual gain errors would depend on the array configuration of a telescope. In this section, we use realistic antenna configurations to estimate the power spectrum bias. To generate the visibilities for a sky with the above source catalog, we use GMRT (Swarup et al., 1991) baseline configuration. However, the methodology followed here can be used to do similar investigations for other arrays. Assuming a circular aperture, 45 meter diameter GMRT dishes project an Airy disk in the sky with the first null of this pattern at $215'$ at 130 MHz. We use the differential source count relation and a uniform position distribution to generate a catalog of 7250 sources in the flux density range 300 μ Jy - 1 Jy within a circular field of view with a radius $200'$. The lower limit of the flux density is comparable to the expected redshifted 21-cm signal strength at 150 MHz. As it is observed that the number of sources of flux densities over 1 Jy is rather lower, we assume to choose a part of the sky where they are not present. We use the differential source count distribution to assign flux density to individual sources. We divide the flux density range into 32 logarithmic bins and estimate the number of sources in each flux bin. We assign flux values for the sources in a given bin randomly within the limits of the bin. This generates a compact source catalog at 150 MHz. We further assign a spectral index to each source in the catalog drawn from a Gaussian distribution with the mean and standard deviation as discussed in section 4.4.1. The distribution of the sources in this catalog is shown in Figure 4.3.

To compare with the expected redshifted 21-cm signal from the EoR, we choose an observation frequency of 130 MHz with a bandwidth of 8 MHz and 128 spectral channels. Figure 4.4 plots the azimuth averaged normalized baseline density of the GMRT at 130 MHz for three different declination angles. The normalization is such that the baseline distribution plotted here is independent of the total number of antennas and the total area in the u-v plane that the array stretches to. The baseline range of the plot reflects the available largest and smallest baselines available with the GMRT. The smallest separation between two GMRT antennas is $\sim$ 100 m, corresponding to a baseline of 0.05 λ.

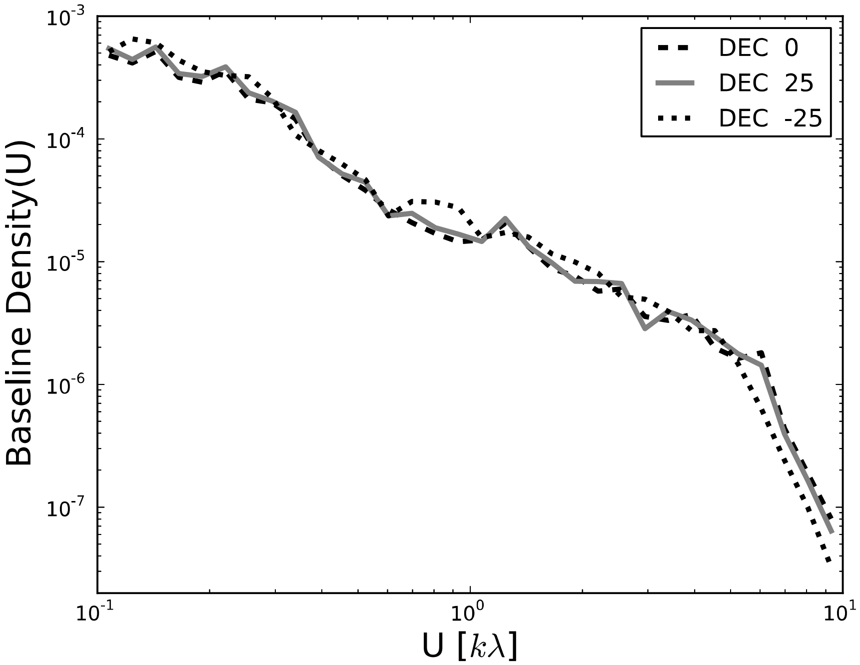

Fig. 4.4 Variation of baseline distribution in uv-space with the different directions in the sky. Baseline density, the number of baselines per unit area at baseline U doesn't change much for different declinations.

Clearly, for baselines larger than 0.1 kλ, the normalized and azimuthally averaged baseline configuration at the GMRT depends weakly on the declination angle of the source. We assume that the source distribution in the catalog discussed above is centered at the right ascension of 0 hour and declination of 25° in the sky. We use the gain model as described in section 4.1 to generate antenna-based time-correlated residual gain errors. Using GMRT baseline configuration at 130 MHz, we use the VCZ (van Cittert, 1934; Zernike, 1938) theorem to simulate 8 hours of observation and generate the visibilities V^S_{AB} for each pair of antenna AB corresponding to the above sky model. We add the effect of the antenna gain to these visibilities to generate the observed visibilities V^M_{AB} and use it for further analysis. Note that, We do not add any instrument noise to the observed visibility in this study.

Assuming that the sky brightness distribution of the compact sources in the sky is already modeled, we estimate the residual visibilities by subtracting V_{AB}^{S} from V_{AB}^{M}. We use the visibility-based power spectrum estimator (equation 4.6) to estimate the power spectrum separately from the residual visibilities for each spectral channel. The mean of the visibility correlation from all the spectral channels gives an estimate of the bias $\mathscr{B}[P](\vec{U})$ in the power spectrum in the presence of residual gain errors. Note that, in the absence of any gain error, the visibility correlation ($V2$) performed with the residual visibilities have a zero mean. In the presence of residual gain errors, the visibility correlation ($V2$) from the residual visibilities measures the bias in the power spectrum.

4.4.3 Results

In our model of residual gain error, we have the parameters α_{δ} and σ_{δ}, which quantifies the amplitude of the residual gain error. The quantifiers for the phase of the gain errors are α_{ϕ} and σ_{ϕ}. The bias in the power spectrum depends on these four parameters. A value of $\alpha = 0$ corresponds to the largest correlation, whereas the gain errors vanish for $\sigma = 0$. We represent the strength of the amplitude gain error σ_{δ} and the phase gain error σ_{ϕ} in percentage and degrees, respectively. We use a range of $(0., 0.1)$ for the σ and a range of $(0.76, 0.97)$ for the α parameters of our model of the gain statistics. These ranges for the σ and α parameters are motivated by the requirement for EoR detection with our model of the gain statistics. In our model, we have neglected the time cross-correlation of the gain errors from different antennae.

Figure 4.5 shows the variation of $\mathscr{B}[P]$ as a function of $\mid \vec{U} \mid$ for $\alpha_{\delta} = \alpha_{\phi} = 0.97$. The dashed line corresponds to $\sigma_{\delta} = 0.06\%,\ \sigma_{\phi} = 0.06^{\circ}$, whereas the dot-dashed lines gives for $\sigma_{\delta} = 0.02\%,\ \sigma_{\phi} = 0.02^{\circ}$. The expected red-shifted 21-cm power spectrum (solid black line) at an observation frequency of 130 MHz is also plotted for comparison (adopted from Bharadwaj and Ali (2005)). With the present calibration techniques the accuracies in the

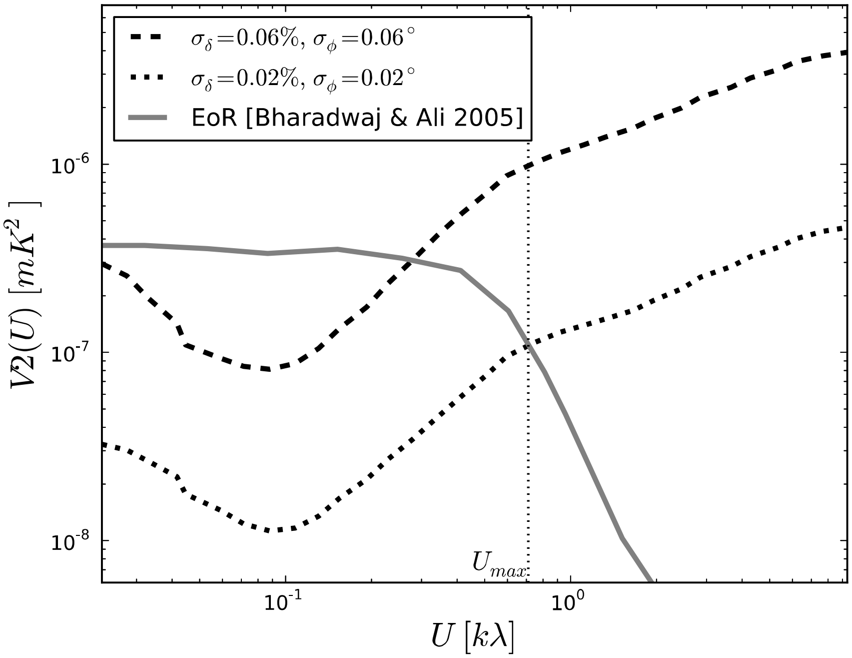

Fig. 4.5 Residual visibility correlation plotted with baseline U. σ_δ is in percentage and σ_ϕ is in degree. U_{max} is the point where bias in the power spectrum exceeds the EoR power spectrum, shown by the vertical dotted line.

visibility amplitude and phase is approximately order of a few percent and a few degrees. So we choose the amplitude error in percentage and phase error in degree and set them equal. Note that, the results quoted henceforth partly depend on the observation frequency chosen above. However, the analysis procedure we adopt in this work can be followed to estimate similar results at other observation frequencies.

The bias in the power spectrum estimator follows a general trend in Figure 4.5, where at a baseline of 0.1 kλ, the bias is minimum and increases monotonically at higher baselines. The rise in the larger baselines can be attributed to a couple of facts. Firstly, the baseline coverage decreases at higher baselines, and hence the chance of having more baseline pairs of type I increases, which in turn increases the bias. In addition, for the higher baselines, the time correlation in the residual gain has larger effects (see section 4.2 for detailed discussion). We also observe that the power spectrum bias increases for baselines smaller than 0.1 kλ. This happens because of the lack of shorter baselines at the GMRT. We expect this effect to be subdominant for the interferometers with better baseline coverage at shorter baselines. This generic trend in the power spectrum bias can be seen in the subsequent figures.

Clearly, at long baselines, the power spectrum bias exceeds the power spectrum of the redshifted 21-cm emission from the H I , and the residual gain errors prevent us from measuring the latter. The power spectrum has a larger bias for larger values of σ parameters. The vertical line marks the largest baseline U_{max} up to which the EoR power spectrum can be estimated in the presence of the residual gain errors for the dot-dashed curve.

At the observation frequency of 130 MHz and at baselines < 0.5 kλ, the redshifted 21-cm signal is almost constant (see figure 4.5). The signal drops to half of its value at the plateau beyond 0.5 kλ. The gain error parameters that give a U_{max} value of 0.5 kλ or larger would allow to estimate the H I signal at these frequencies.

To see the variation of U_{max} with the σ parameters we use a fiducial value of $\alpha_\delta = \alpha_\phi = 0.97$ and estimate the value of U_{max} for different values of σ_δ and σ_ϕ. Grey contours in Figure 4.6 give the values of U_{max} for variation of σ parameters between $0-0.1$. Note that U_{max} gives the maximum baseline to which the bias in the power spectra is lower than the power spectra itself. Hence U_{max} gives the maximum baseline to which the power spectra can be estimated for each parameter value (σ, α). A higher value of σ corresponds to a higher residual gain error and hence is expected to provide more bias in the power spectra. It is then expected that as σ increases, the maximum baseline to which the 21-cm signal extraction is possible, i.e., U_{max}, decreases. This is exactly the nature we see in Figure 4.6. At higher gain errors, the 21-cm signal extraction is severely restricted. We have used an empirical function to fit the contours, and the best fit is shown with dark dashed lines. Details of this empirical fit can be found in Appendix A.

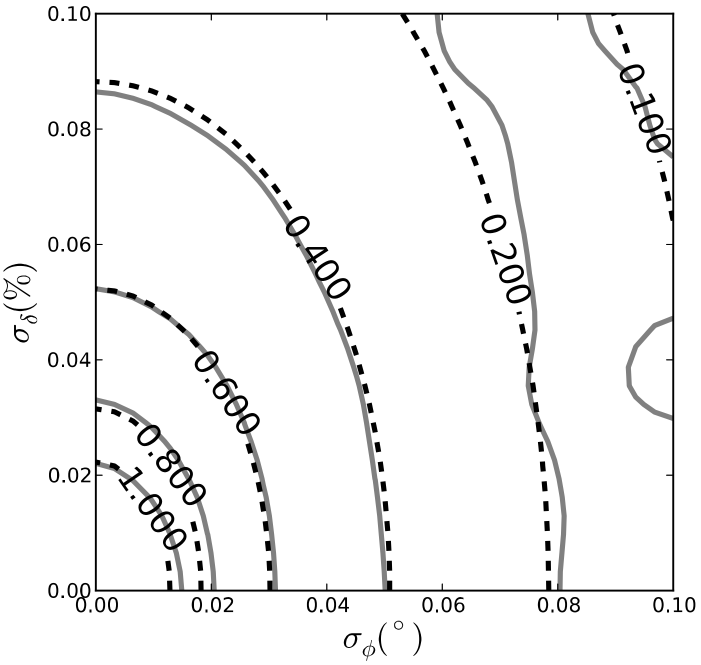

Fig. 4.6 This contour plot is showing the variation of U_{max} as a function of residual amplitude and phase gain errors. The maximum allowed baseline length U_{max} in kilo wavelengths is written over contour plots. Here amplitude gain errors σ_δ and σ_ϕ (radian) are given in percent and degree respectively. The values of $\alpha_\delta = \alpha_\phi = 0.97$.

Figure 4.7 shows the variation of the U_{max} with respect to the α parameters for a range $0.76-0.97$. We have kept both the σ parameters fixed at 0.02. The grey contours show the values of the U_{max} as calculated from the simulation. The dark dashed curves are the result of an empirical fit to the simulation results (see Appendix A). The residual gain errors are more correlated for lower values of α parameters. Hence, for lower values of α parameters, we expect the bias in the power spectra to exceed the 21-cm signal at lower baselines. This results in a lower value of the maximum baseline, U_{max}, to which the 21-cm signal extraction is possible. This explains why for lower values of α in Figure 4.7 , values of U_{max} are lower.

We estimate the power spectral gain $\mathscr{G}(U)$ (see equation 4.15) for different values in our parameter space. Figure 4.8 show the the variation of $\mathscr{G}(U)$ with baseline for σ and

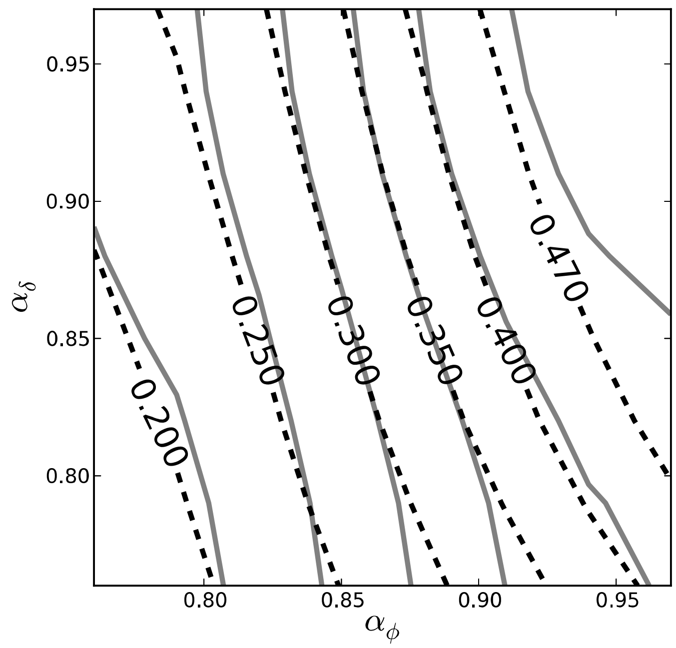

Fig. 4.7 Contour plot showing the variation of U_{max} in kilo wavelengths with the α parameters. The grey solid line corresponds to results from the simulation and the dark dashed lines are an empirical fit to the simulation. Values of the σ parameters fixed at 0.02.

α parameter combinations of $[0.02, 0.06]$ and $[0.95, 0.97]$ respectively. Since the quantity $\mathscr{G}(U)$ is independent of the foreground model, the estimates of the $\mathscr{G}$ can be used to calculate the bias in the power spectrum for any foreground model.

4.5 Discussion and Conclusion

In this work, we addressed the effect of residual gain errors in interferometric calibrations to estimate the power spectrum of the sky brightness fluctuations for high dynamic range observations. Our particular focus has been the estimation of the power spectrum of the redshifted 21-cm signal in the presence of bright galactic and extragalactic foregrounds. We considered a point source foreground model where exact visibility-based foreground

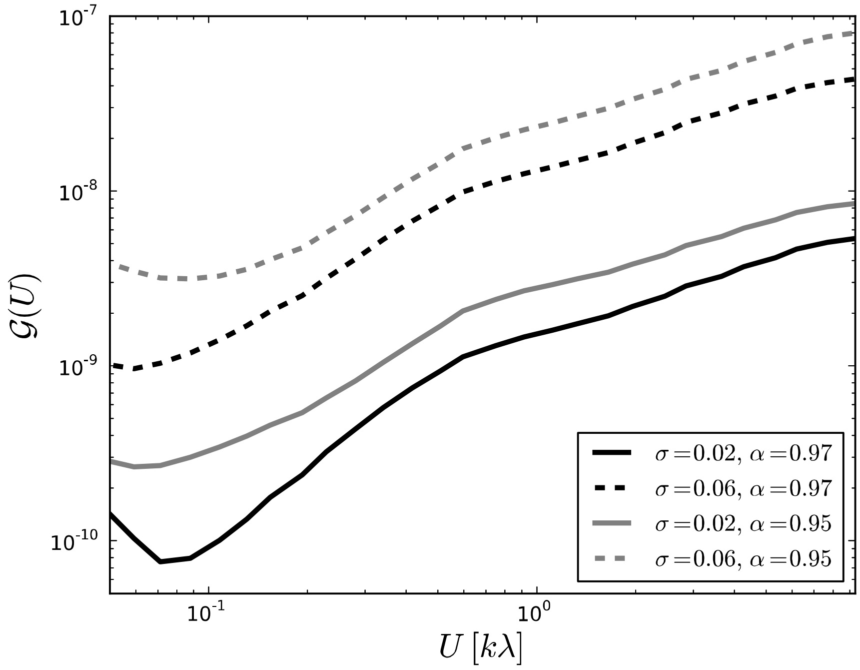

Fig. 4.8 The ratio of the bias to the power spectrum $\mathscr{G}(U)$ for point source sky for different residual gain errors.

subtraction is possible. We see, however, that even with a known foreground model, the estimated power spectrum will have bias coming through the residual gain errors. We investigated analytically the origin of the bias in the power spectrum in the presence of residual gain errors through different types of baseline pairs used in the visibility correlation. To understand the effect of the residual gain errors on the bias in the power spectrum in a more realistic scenario, we simulate visibilities for a sky with compact sources in the presence of residual gain errors. We choose a power-law function to model the time correlation in the amplitude and the phase of the residual gain errors. The important findings of this analysis are

- We discuss a methodology to assess the effect of time-correlated residual gain errors in the presence of bright foreground. Using simulated observations with the GMRT-like array configurations, we found that for the nearby baseline visibility correlation estimators, the residual gain errors result in a scale-dependent bias in the estimates of the power spectrum. This effect adds to the systematics in the detection of the faint redshifted 21-cm signal.

- The bias originates when a pair of baselines are used in the visibility correlation that has at least one antenna in common. The majority of the bias arises from the correlations done with baselines involving the same antenna pairs. Analytical calculations followed by investigations with simplistic toy models of gain errors show that the main reason for the bias is the time correlation in the residual gain errors. The bias additionally depends on the baseline distribution of the particular interferometers.

- The bias is found to increase with the standard deviation of the gain errors. It is also observed that an increase in the time correlation also increases the bias. The gain errors in the amplitude and the phase contribute approximately in a similar way to the bias.

- The bias depends highly on the calibration accuracy. Figure 4.10 suggests that we may reduce the bias either by observing the signal over a larger number of days or by increasing the calibration accuracy. However, now it is understood that owing to the correlated point error, mechanical beam modulation, and time stability of the beam, the gain errors over different days can still be correlated and may introduce additional effects. In this view, it seems that more accurate calibration is the key to reducing the bias and detecting the 21-cm signal using nearby baseline visibility correlation techniques.

As discussed earlier, the power spectral gain $\mathscr{G}(\vec{U})$ carries the effect of the residual gain errors. It is independent of the foreground model and hence, can be used to estimate the bias in the power spectrum in the presence of any foreground model. We use this power

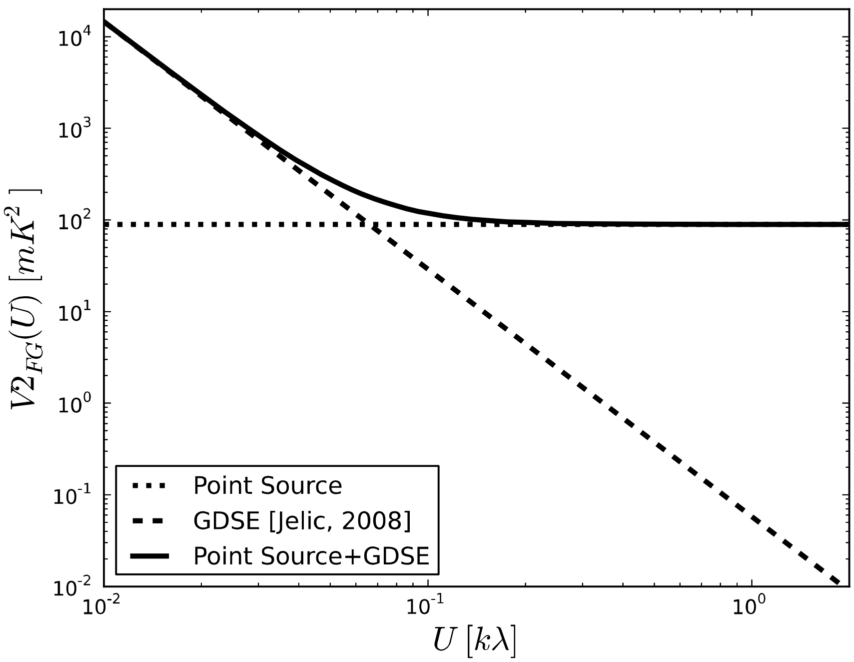

Fig. 4.9 Power spectrum for different components of the foreground. The dot-dashed line is the Poisson component of point sources used in this paper, the dashed line corresponds to the galactic diffuse synchrotron emission (GDSE) (Jelić et al., 2008). The solid curve integrates the effect of both foreground components.

spectral gain to estimate the bias in the presence of extragalactic point sources as well as the galactic diffuse synchrotron emission.

The solid black line in Figure 4.9 shows the expected foreground power spectrum in the presence of the point source model we used here (dot-dashed line) and the diffuse galactic foreground at 130 MHz (Jelić et al., 2008) (black-dashed line). We use this full foreground model and the estimated power spectral gain $\mathscr{G}(\vec{U})$ to plot the bias in the power spectrum (black dashed line) for 1000 hours of observation with the GMRT baseline configuration in Figure 4.10. Here we have assumed that the gain errors do not have any long time correlation, and they are completely uncorrelated for different days. The σ parameters of the gain errors are set to fiducial values of 1.0, and the α parameters are set to 0.97. This value of the α corresponds to a low time correlation. This choice of the σ parameter

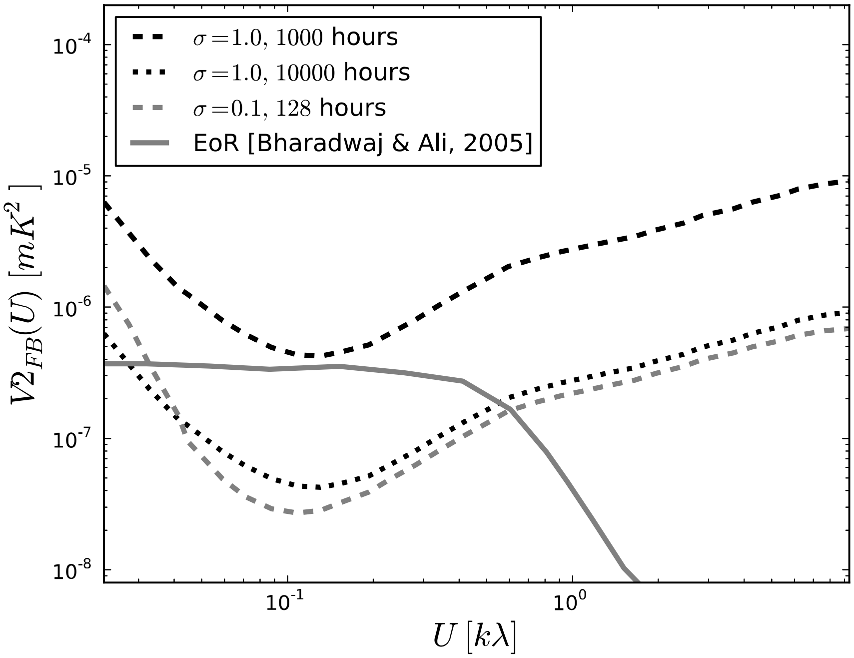

Fig. 4.10 Bias in the power spectrum with a compact and diffuse foreground model in the presence of different residual gain error models and observation time. The α parameters are kept at a fiducial value of 0.97 for all gain error models. The black dashed line corresponds to σ parameters of unity and an observation time of 1000 hours. The black dot-dashed line corresponds to the same gain error model but with 10000 hours of observation time. The grey-dashed line corresponds to σ parameter set to 0.1 and 128 hours of observation only. The grey solid line is the redshifted 21-cm signal (Bharadwaj and Ali, 2005) expected at 130 MHz.

corresponds to a 1% error in the gain amplitude and 1° in the phase. The dot-dashed line in Figure 4.10 corresponds to the bias in the power spectrum with the same foreground and gain model with 10000 hours of the GMRT observations and is below the expected 21-cm signal (solid grey line, adopted from Bharadwaj and Ali (2005)) at the usable range of baselines. A reduction in the power spectrum bias is expected with only 128 hours of observations with a calibration accuracy corresponding to 0.1% error in the gain amplitude and 0.1° in the phase (grey dashed line in Figure 4.10).

In this work, we assume that the gain errors are drawn from a time-correlated Gaussian distribution. The auto-correlation function of the individual antenna gain errors is assumed to follow a power law. We use this model of gain statistics in our methodology to estimate the power spectrum bias. We note here that for a given interferometer, careful observation has to be used to establish the gain statistics first. The calibration requirements to observe the EoR signal can then be evaluated for the particular interferometer using its gain statistics. We also have neglected the time cross-correlation of the gain errors from different antennae. As the self-calibration-based gain solution for the phase uses three antennae for the phase closure, hence, the phase solution of the three antennae involved in the phase closure can apparently be correlated. However, such phase solutions are obtained for all possible triads of antennae with a given common antenna and then averaged over. Hence, it is expected the cross-correlation of gain between two antennae is rather small compared to the self-correlation. A similar argument can be evoked for the self-calibration solutions of the amplitude gains, where the closure requires four antennae. Ewall-Wice et al. (2017) use the analytical calculation to show that the gain auto-correlation varies roughly as the inverse of the number of the antenna in the array, whereas the cross-correlation of gain between different antennae varies as the inverse of the square of the number of antennas. These arguments show that to the first approximation, we can neglect the cross-correlation of gain between different antennas. The contribution to different baseline pair fractions in the power spectrum bias has to be recalculated if the cross-correlation of the antenna gain from the different antennae is significant.

In this work, we estimate the effect of residual gain error at different baselines for visibility correlation done at a given channel. This corresponds to the estimation of the 21-cm power spectrum as a function of the wave-number perpendicular to the line of sight and integrated over all the wave numbers parallel to the line of sight. We have assumed that the residual gain errors are not correlated across different frequency channels. In a realistic scenario, the frequency dependence of the gain is calibrated by estimating the bandpass response of the instrument (Taylor et al., 1999). The estimation of the bandpass response is often done using a polynomial model, which can induce correlated residual gain errors in the bandpass response. This is expected to add to the effect of the foreground wedge when the power spectrum of the 21-cm signal is estimated in the 2D wave-number plane (Datta et al., 2010; Morales et al., 2012; Parsons et al., 2012; Vedantham et al., 2012). However, since the 21-cm signal from a given redshift decorrelates faster with frequency (Bharadwaj and Ali, 2005; Bharadwaj and Pandey, 2003) than the foreground signals, the effect of frequency dependence in the residual gain errors is not straightforward to estimate. It has been observed in the literature that for the spectrally smooth gain solutions, the bias in the power spectrum estimator is relatively less significant (Barry et al., 2016; Ewall-Wice et al., 2017; Trott and Wayth, 2016). It is still important to investigate, for the nearby baseline visibility correlation estimators, how much variation in the calibration errors in frequencies affects the power spectrum bias.

The standard deviation of the power spectrum estimator is also expected to change in the presence of residual gain errors. This would add to the statistical risk in the 21-cm power spectrum estimator. We discuss the change in the variance of the power spectrum due to the presence of residual gain errors in the next chapter of this thesis. The effect of frequency-dependent gain errors will also be discussed in subsequent chapters.

****